Review of Materials Research 1 (2025) 100004

Contents lists available at ScienceDirect

Review of Materials Research

journal homepage: www.sciencedirect.com/journal/review-of-materials-research

Active learning prediction and electromagnetic levitation measurement of metastable liquid properties of Ti-Al-Zr alloy

R.L. Xiao, K.L. Liu, H.R. Li, Y. Ruan *

MOE Key Laboratory of Materials Physics and Chemistry under Extraordinary Conditions, Northwestern Polytechnical University, Xi' an, 710072, China

ARTICLE INFO

Keywords:
Active learning
Neural network
Thermophysical properties
Liquid local structure
Molecular dynamics

ABSTRACT

The accurate knowledge of liquid properties for Ti-Al based alloys is of great significance for scientific explorations such as revealing the atomic-scale behaviors in alloy processing and realizing the optimization of manufacture technology. By means of the active learning method based on deep neural network (DNN) and electromagnetic levitation technology (EML), we investigate the microstructure evolution of $Ti_{47}Al_{47}Zr_6$ alloy, and with a focus on obtaining its liquid state properties. The density, surface tension, viscosity of this liquid alloy and the related self-diffusion coefficient are predicted by the DNN potential. The calculated surface tension exhibits only a deviation of less than 2 % as compared with EML experimental values. The liquid local structure characteristics acquired through Voronoi polyhedron analysis indicate that the fraction of relatively high-coordinated clusters with Al as the central atom displayed an anomalous decrease with the falling of liquid temperature. This effect is attributed to the tendency of these clusters to form icosahedral-like geometries, resulting in an increased fraction of icosahedral-like geometries in liquid alloy.

1. Introduction

Considering their low density, high specific strength, ablation resistance, good high-temperature mechanical properties, and excellent oxidation resistance, Ti-Al based alloys are an emerging type of materials for aviation and aerospace field [1,2]. They have been applied in critical high-temperature components such as skin and control surface of spacecraft, and aircraft engine blade [2–5]. Researchers have made efforts to improve the service performance of Ti-Al based alloys, but further advancements are still needed [6,7]. Precise determination of the liquid thermophysical properties is essential for optimizing the manufacturing processes, and understanding the liquid structure is helpful in revealing its liquid-solid phase transition process, thereby further realizing performance optimization. In experimental studies, researchers utilized ground-based or space station electromagnetic levitation (EML) facilities to investigate the thermophysical properties of Ti-Al, Ti-Al-Nb, Ti-Al-Ta and Ti-Al-Cr-Nb alloys [8–11]. Also, *in situ* synchrotron micro X-ray diffraction was employed to study the liquid-solid phase transition process of Ti-Al alloys [12]. In simulations, *ab-initio* molecular dynamics (AIMD) simulations based on density functional theory (DFT) was conducted to explore the influence of chemical composition on the thermodynamic properties and liquid structure of Ti-Al alloys [13]. Additionally, researchers have developed empirical interatomic potentials for classical molecular dynamics (MD) of Ti-Al [14], Ti-Al-Nb [15], and Ti-Al-Ni [16] alloys based on the solid phase, although further validation of their prediction accuracy for liquid alloys is still required.

While experimental measurements and first-principles calculations are reliable, they often come with high costs and low efficiency. Classical molecular dynamics simulations are efficient, while they may have slightly lower accuracy. Advances in machine learning methods, such as deep neural network (DNN), have provided researchers with a promising approach to obtaining properties of materials [17–19], striking a balance between accuracy and efficiency.

In this work, we consider the beneficial effects of Zr on the mechanical properties, oxidation resistance, irradiation resistance, as well as processability and weldability of Ti-Al alloys [20–22], and select Ti-Al-Zr alloy as the research subject. The microstructure and phase constitution of rapid solidified Ti-Al-Zr alloy are analyzed. By active learning approach based on Deep Potential Generator (DPGEN) [23], DNN potential for liquid Ti-Al-Zr alloy is constructed to acquire its thermophysical properties. Moreover, the structural evolution behavior in the liquid alloy is revealed.

* Corresponding author.
E-mail address: ruany@nwpu.edu.cn (Y. Ruan).

https://doi.org/10.1016/j.revmat.2025.100004
Received 21 March 2025; Received in revised form 1 April 2025; Accepted 1 April 2025
Available online 3 April 2025

2. Experiments and simulations

The electromagnetic levitation (EML) technology [24] was used for rapid solidification of the alloy and to measure the surface tension of the liquid alloy. Prior to the EML experiments, the $Ti_{47}Al_{47}Zr_6$ master alloy was prepared from pure Ti (99.999 %), pure Al (99.999 %), pure Zr (99.99 %), using an arc melting furnace. In the EML experiments, the chamber was evacuated to a high vacuum environment (10^{-4} Pa) and then backfilled with a mixture gas of high purity Ar (99.999 %), He (99.999 %), and H_2 (99.999 %) in the volume ratio of 10:9:1 to prevent oxidation. The temperature of the EML sample was monitored by a KELLER CellaTemp PA20 pyrometer. After the experiments, the samples were analyzed by an FEI Verios G4 scanning electron microscope (SEM), a Bruker D8 Discover A25 X-ray diffractometer (XRD), and an FEI Themis Z double Cs corrector transmission electron microscope (TEM).

A total of 3.90×10^4 configurations served as the initial training dataset were obtained by performing AIMD calculations using the Vienna *ab initio* simulation program (VASP). These calculations were conducted for liquid pure Ti at 1300, 1800, and 2500 K; liquid pure Al at 800, 1200, 1800, and 2500 K; liquid pure Zr at 1400, 1800, and 2500 K; and the liquid middle-entropy alloy $Ti_{34}Al_{33}Zr_{33}$ at 1200, 1800, and 2500 K. During the AIMD calculation, the Projector-Augmented-Wave (PAW) pseudopotentials and Perdew-Burke-Ernzerhof (PBE) gradient approximation to the exchange-correlation functional were adopted to predict the system evolution. Only the Γ point was used to sample the Brillouin zone, and the energy cutoff of 300 eV was set. The systems were conducted under periodic boundary conditions and canonical (NVT) ensemble with the Nosé-Hoover thermostat (200 atoms in the supercell, time step 3 fs and external pressure 0 ± 3 kbar).

After the initial training dataset was prepared, the DPGEN was employed to automatically generate DNN potential for the liquid $Ti_{47}Al_{47}Zr_6$ alloy through 10 Training-Exploration-Labeling iterations. The fundamental principles and methods of DPGEN have been introduced in Refs. [23,24]. During the exploration process of the 10 iterations, the DPGEN software was used to freely explore the evolution of the liquid $Ti_{47}Al_{47}Zr_6$ alloy with 40 initial structures within the temperature range of 1300–2500 K. In the labeling process, the lower boundary and upper boundary of the force differences [ε_{low}, ε_{high}], were set to [0.15, 0.30] eV·Å^{-1}. In each iteration's labeling process, the DPGEN software randomly selected up to 2000 configurations labeled as "Candidate" for AIMD calculations, which were then added to the training dataset in the subsequent iteration's training process. Throughout the active learning process, a total of 2×10^4 configurations were actively added to the training dataset. In each training process, four DNN potentials was generated, the cutoff radius was 6 Å, and the smooth started from 5.8 Å. The embedding and fitting nets had (25, 50, 100) and (240, 240, 240) layers, respectively. The training was performed for 1×10^6 epochs with an exponentially decaying learning rate from 1×10^3 to 3.51×10^{-8} using an NVIDIA TESLA V100 TENSOR CORE GPU. Subsequently, the properties of the liquid $Ti_{47}Al_{47}Zr_6$ alloy were acquired through MD simulation in LAMMPS by DNN potential. The MD simulation involved a supercell containing 8100 atoms, which was equilibrated at the set temperature using the isothermal-isobaric (NPT) ensemble with a time step of 1 fs. The cooling rate was 10^{12} K s^{-1}.

3. Results and discussion

3.1. Microstructure and phase constitution

Before acquiring the liquid properties, the microstructure and phase constitution were analyzed, as shown in Fig. 1. The XRD pattern indicated the presence of the γ-TiAl phase in the alloy. However, the α_2-Ti_3Al phase only exhibited two peaks, making it impossible to determine its existence. Therefore, TEM analysis was further conducted. Ultimately, by combining the Ti-Al phase diagram, SEM image of arc-melted $Ti_{47}Al_{47}Zr_6$ master alloy, selected area electron diffraction (SAED) patterns and XRD result (Fig. 1a), the phase transformation path can be inferred. During the cooling period, the αTi phase was first formed from the liquid alloy, and then the residual liquid phase evolved into γ phase. Eventually, the αTi phase underwent eutectoid transition and transformed into the γ phase and α_2 phase. Moreover, the SAED illustrated that the (γ+α_2) eutectoid followed the Blackburn orientation relationship: $(111)_\gamma//(0001)_{\alpha 2}$, $[1\bar{1}0]_\gamma//[11\bar{2}0]_{\alpha 2}$. In the EML experiments, the $Ti_{47}Al_{47}Zr_6$ alloy achieved a maximum undercooling of up to 277 K ($0.16T_L$). The microstructure of alloy solidified with $\Delta T = 277$ K is demonstrated in Fig. 1b. The phase composition of the alloy with 277 K undercooling remained consistent with that of the master alloy, while the primary αTi dendrites were refined and the formation of interdendritic γ phase was inhibited.

3.2. Validation for DNN potential

Fig. 2a is the variation in the fraction of labeled data during the active learning process. In the iteration 0, since the initial training dataset did not include configurations of the liquid $Ti_{47}Al_{47}Zr_6$ alloy, and the compositions of the configurations in the initial training dataset were far from the $Ti_{47}Al_{47}Zr_6$ alloy in the phase diagram. As a result, the fractions of configurations labeled as "Accurate", "Candidate", and "Failed" during the evolution of the liquid $Ti_{47}Al_{47}Zr_6$ alloy calculated by the four models were 0 %, 66.37 %, and 33.63 %, respectively. As the number of iterations increased, the DPGEN software continuously added new configurations to the training dataset, leading to a rapid increase in the fraction of data labeled as Accurate, while the quantities of data labeled as Candidate and Failed decreased significantly. By the iteration 9, the fraction of data labeled as Accurate reached 90.23 %, while the fraction

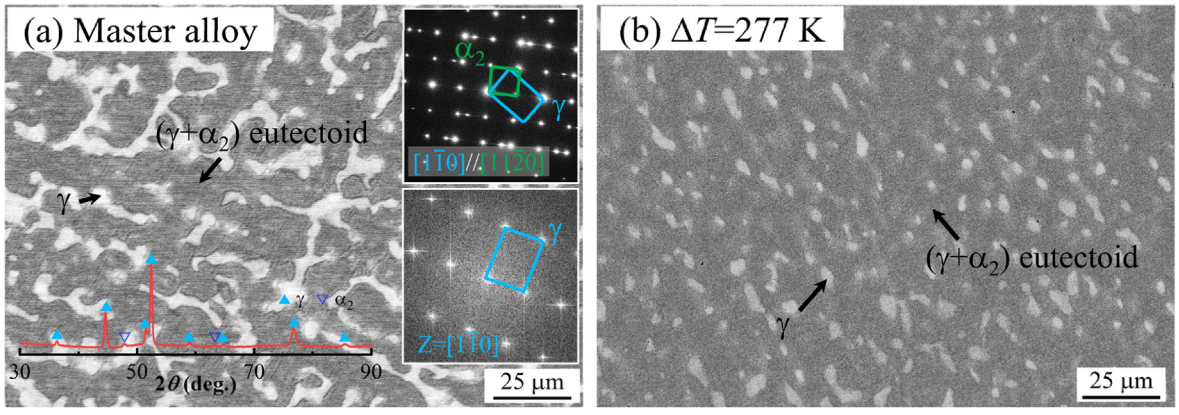

Fig. 1. Microstructure and phase analyses of $Ti_{47}Al_{47}Zr_6$ alloy: (a) master alloy [insets represent XRD pattern of master alloy and SAED patterns of (γ+α_2) eutectoid and γ phase]; (b) alloy solidified with 277 K undercooling.

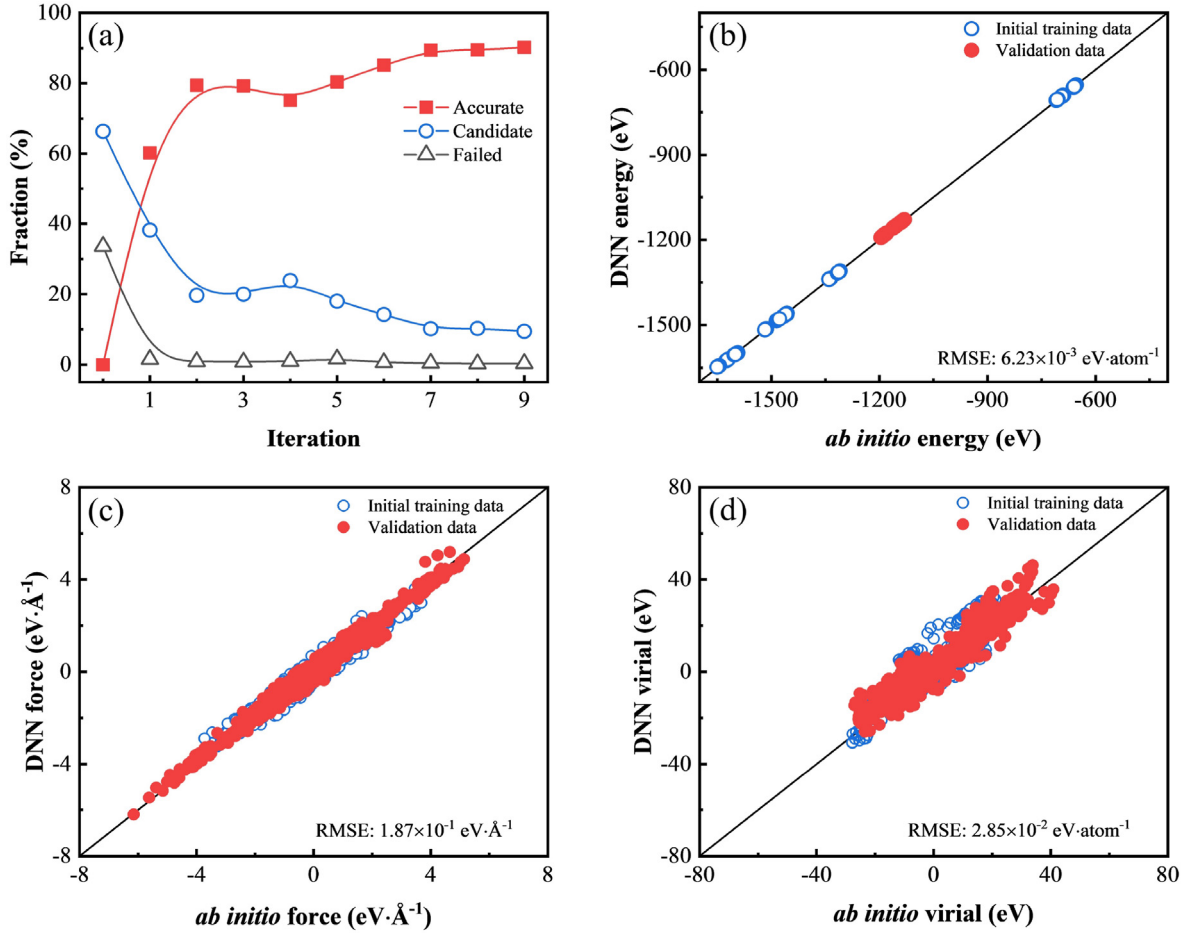

Fig. 2. DNN potential accuracy validation: (a) data fraction versus iteration in active learning process; (b) energy; (c) force; (d) virial.

labeled as Failed dropped to 0.34 %. This indicated a high consistency in the predictions of the four models regarding the evolution process of the liquid $Ti_{47}Al_{47}Zr_6$ alloy after the iteration 9. Owing to the high consistency among the four models, theoretically, anyone of them can be selected as the DNN potential for the liquid $Ti_{47}Al_{47}Zr_6$ alloy. One of the models was randomly chosen, and its predictive accuracy was examined, as shown in Fig. 2b and c. The validation datasets consisted of the liquid $Ti_{47}Al_{47}Zr_6$ systems at 2500, 2000, 1500 and 1300K, respectively, which were not included in the training dataset. The DNN potential provided energy, atomic forces, and virial results that aligned well with those from AIMD, with root mean square errors (RMSEs) in orders of 10^{-3} eV·atom^{-1} for energy, of 10^{-1} eV Å^{-1} for atomic force, and of 10^{-2} eV·atom^{-1} for virial. Moreover, during the predicted liquid evolution process, no unphysical atomic aggregation or stratification behavior was observed [see example snapshot in Fig. 3a]. And the predicted pair distribution functions (Fig. 3b) and bond angle distributions (Fig. 3c) of the liquid alloy by the DNN potential also matched well with the AIMD results, indicating that the DNN potential achieved computational accuracy comparable to DFT for the liquid alloy.

3.3. Liquid properties

After examining the DNN potential, the thermophysical properties of the liquid $Ti_{47}Al_{47}Zr_6$ alloy were calculated in LAMMPS by utilizing the DNN potential. The surface tension σ_L of the alloy calculated by DNN potential exhibited a liner dependency on temperature, as shown in Fig. 4a, and can be described by the following equation:

$$\sigma_{L,DNN} = 1.25 - 2.46 \times 10^{-4}(T - T_L). \quad (1)$$

The surface tension measured by EML can be expressed as

$$\sigma_{L,EML} = 1.23 - 3.38 \times 10^{-4}(T - T_L). \quad (2)$$

The measured results showed a deviation of only less than 2 % as compared with the calculated values across the entire experimental temperature range, indicating that the DNN potential demonstrated a high level of accuracy in predicting thermophysical properties of the alloy. The density ρ_L (Fig. 4b) was further calculated, and its relationship with temperature can be expressed as

$$\rho_{L,DNN} = 3.62 - 2.56 \times 10^{-4}(T - T_L). \quad (3)$$

The viscosity η_L (Fig. 4c) of the liquid alloy and self-diffusion coefficient D_L (Fig. 4d) of Ti, Al, and Zr in the liquid alloy predicted by DNN potential exhibited an exponential variation with decreasing temperature and can be fitted as

$$\eta_{L,DNN} = 0.04 \exp\left(\frac{7.31 \times 10^4}{R_g T}\right), \quad (4)$$

$$D_{L,Ti} = 2.24 \times 10^{-7} \exp\left(\frac{-6.44 \times 10^4}{R_g T}\right), \quad (5)$$

$$D_{L,Al} = 2.61 \times 10^{-7} \exp\left(\frac{-6.46 \times 10^4}{R_g T}\right), \quad (6)$$

$$D_{L,Zr} = 1.96 \times 10^{-7} \exp\left(\frac{-6.50 \times 10^4}{R_g T}\right). \quad (7)$$

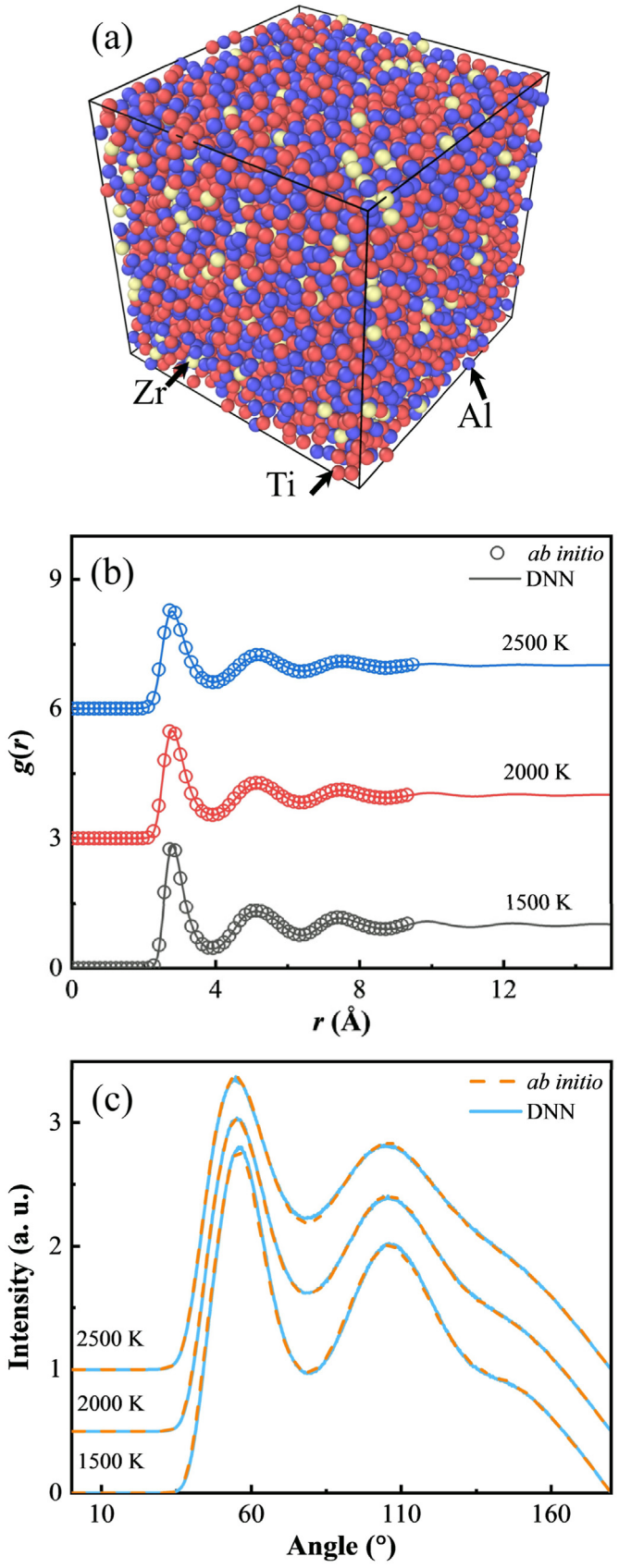

Fig. 3. Liquid structure characteristics of $Ti_{47}Al_{47}Zr_6$ alloy: (a) snapshot of liquid alloy at 2500 K (Ti, red; Al blue; and Zr, yellow); (b) pair distribution functions; (c) bond angle distributions.(For interpretation of the references to colour in this figure legend, the reader is referred to the web version of this article.)

Voronoi polyhedron analysis was adopted to reveal the liquid local structure evolution of the $Ti_{47}Al_{47}Zr_6$ alloy. The Voronoi indices $< n_3, n_4, \ldots, n_i >$ represent the number of polyhedron faces with i edges, and the sum of n_i is equivalent to the coordination number (CN) of the central atom. The fraction of 10 most abundant Voronoi polyhedrons in the liquid alloy and CNs of different central atoms were counted and presented in Fig. 5. The analysis revealed that clusters with CN = 12 and 13, characterized as icosahedral (ICO, <0, 0, 12, 0>), distorted ICO (<0, 2, 8, 2> and <0, 1, 10, 2>), and quasi-icosahedral geometries (<0, 2, 10, 0>, <0, 4, 6, 2>, <0, 3, 6, 4>, <0, 3, 8, 2>, <0, 4, 6, 3>, <0, 3, 7, 3>, and <0, 2, 10, 1>), dominated the liquid alloy, and their population increased as the temperature decreased. This indicated that as the temperature decreased, the interaction between various atoms strengthened and the atoms tended to form bonds, leading to enhanced liquid local structural stability, which eventually resulted in an increase in the surface tension, density and viscosity of the liquid alloy, while the atomic diffusion ability decreased. Clusters with CN = 14 and CN = 16 predominantly characterized the local environments around Ti and Zr atoms, respectively. The fraction of relatively high-coordinated clusters (full line) increased as the temperature decreased, while the fraction of relatively low-coordinated clusters (dash line) exhibited an inverse correlation with temperature, specifically in the clusters with Ti and Zr as the central atoms. This demonstrated that as the temperature decreased, the low-coordinated clusters with loose correlations tended to transform into high-coordinated cluster with tight correlations. It is noteworthy that in the clusters with Al as the central atom, the fraction of relatively low-coordinated clusters with CN = 12, 13, and 14 increased, while the fraction of the high-coordinated clusters with CN = 15 and 16 decreased. This behavior was completely opposite to that observed in the clusters with Ti and Zr as central atoms. This phenomenon can be attributed to the tendency of Al-centered clusters to favor ICO-like geometries, which was reflected in the increasing fraction of ICO-like geometries in the liquid alloy as the temperature decreased.

4. Conclusions

In summary, this work utilized active learning method to construct a DNN potential for the $Ti_{47}Al_{47}Zr_6$ alloy, enabling accurate prediction of its liquid properties. Meanwhile, the surface tension of this liquid alloy was measured by EML experiments for a comparison. The following conclusions are derived.

(1) The arc-melted master alloy and the EML sample consist of (γ+α_2) eutectoid structures formed by the decomposition of primary αTi dendrite, along with the interdendritic γ phase. The primary αTi dendrites were refined under rapid solidification condition.

(2) The DNN potential achieved accuracy levels comparable to DFT in predicting system energy, atomic forces, virial, and liquid structure. The surface tension of the liquid alloy is 1.25 N m^{-1}, the density is 3.62 g cm^{-3} and the viscosity is 6.68 mPa s at the liquidus temperature. Within the temperature range of 1300–2500 K, the surface tension and density exhibit a linear variation, while the viscosity and self-diffusion coefficient show an exponential change. The calculated surface tension displays only a deviation of less than 2 % as compared with the EML experimental values.

(3) As the temperature of the liquid alloy decreases, the low-coordination clusters with Ti and Zr as central atoms tend to transform into high-coordination clusters. In contrast, in those clusters with Al as the central atom, there appears to be an increase of clusters with coordination numbers of 12, 13 and 14. This ultimately results in the formation of a significant number of icosahedral-like geometries in liquid alloy.

CRediT authorship contribution statement

R.L. Xiao: Writing – original draft, Visualization, Methodology,

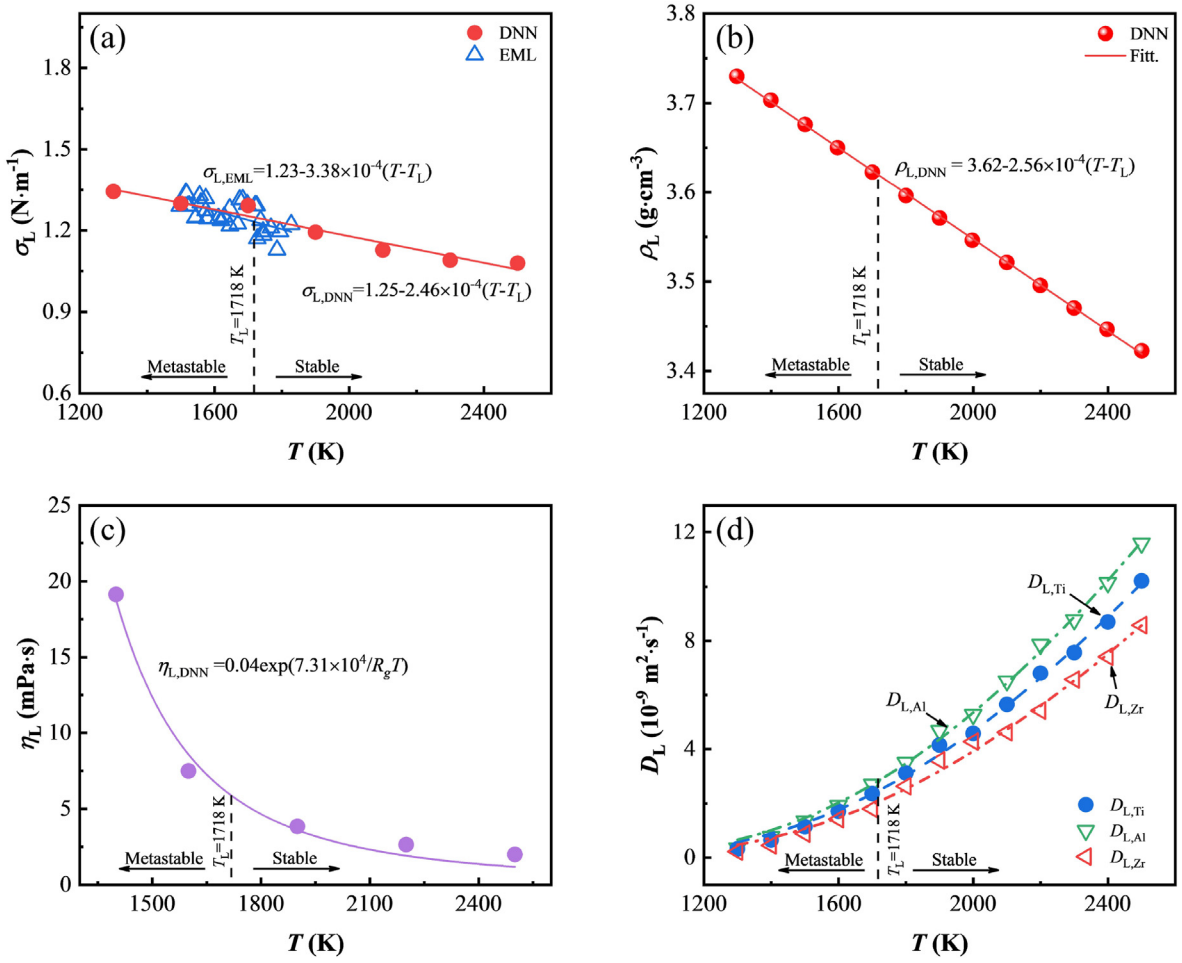

Fig. 4. Thermophysical properties of liquid $Ti_{47}Al_{47}Zr_6$ alloy: (a) surface tension; (b) density; (c) viscosity; (d) self-diffusion coefficient.

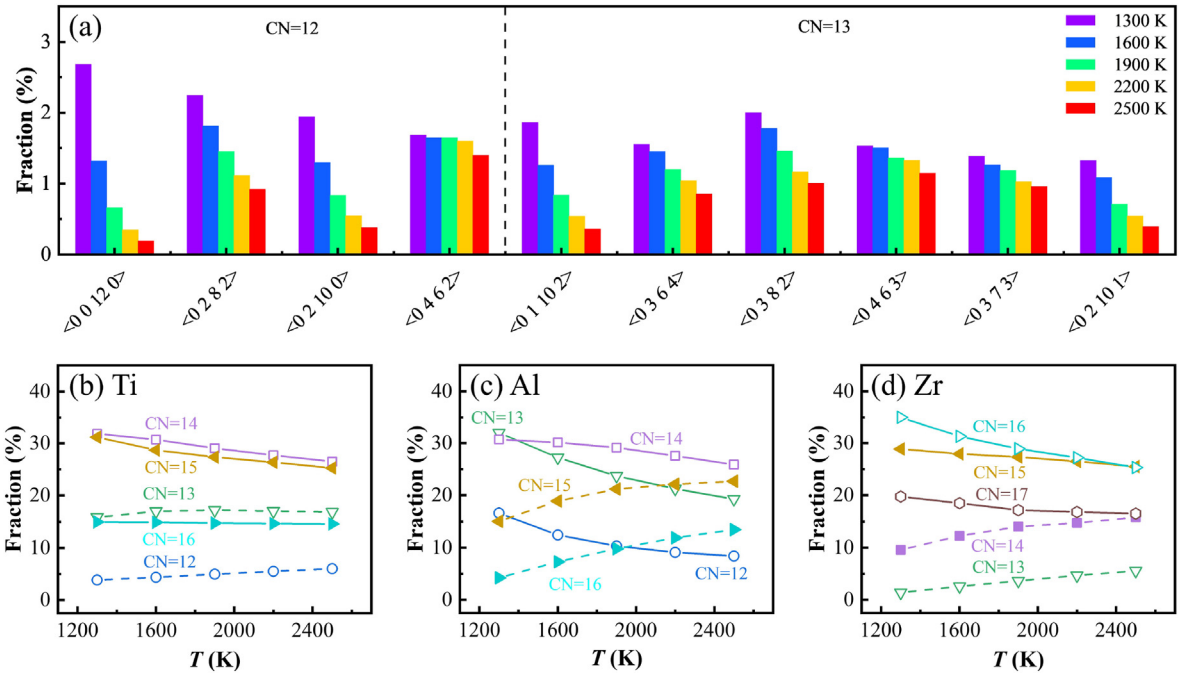

Fig. 5. Liquid local structure characteristics of $Ti_{47}Al_{47}Zr_6$ alloy: (a) fraction of Voronoi polyhedrons; (b) fraction of CN for Ti; (c) fraction of CN for Al; (d) fraction of CN for Zr.

Investigation, Formal analysis, Conceptualization. **K.L. Liu:** Validation, Methodology, Formal analysis. **H.R. Li:** Methodology, Formal analysis. **Y. Ruan:** Writing – review & editing, Supervision, Investigation, Funding acquisition, Conceptualization.

Declaration of competing interest

The authors declare that they have no known competing financial interests or personal relationships that could have appeared to influence the work reported in this paper.

Acknowledgements

This work was supported by the National Natural Science Foundation of China (Grant Nos. 52225406, 52073232, and 52088101), and the Space Application System of China Manned Space Program. The authors thank Dr. L. Y. Li and Mr. C. H. Sun for their helpful discussions.

References

[1] T. Klein, L. Usategui, B. Rashkova, M.L. Nó, J. San Juan, H. Clemens, S. Mayer, Mechanical behavior and related microstructural aspects of a nano-lamellar TiAl alloy at elevated temperatures, Acta Mater. 128 (2017) 440–450, https://doi.org/10.1016/j.actamat.2017.02.050.

[2] G. Zheng, B. Tang, S. Zhao, W.Y. Wang, X. Chen, L. Zhu, J. Li, Evading the strength-ductility trade-off at room temperature and achieving ultrahigh plasticity at 800°C in a TiAl alloy, Acta Mater. 225 (2022) 117585, https://doi.org/10.1016/j.actamat.2021.117585.

[3] B. Selvarajou, M.H. Jhon, R.V. Ramanujan, S.S. Quek, Temperature dependent anisotropic mechanical behavior of TiAl based alloys, Int. J. Plast. 152 (2022) 103175, https://doi.org/10.1016/j.ijplas.2021.103175.

[4] N. Takata, K. Uematsu, M. Kobashi, Compressive properties of porous Ti–Al alloys fabricated by reaction synthesis using a space holder powder, Mater. Sci. Eng., A 697 (2017) 66–70, https://doi.org/10.1016/j.msea.2017.05.015.

[5] F. Appel, H. Clemens, F.D. Fischer, Modeling concepts for intermetallic titanium aluminides, Prog. Mater. Sci. 81 (2016) 55–124, https://doi.org/10.1016/j.pmatsci.2016.01.001.

[6] Y. Sun, Z. Wan, L. Hu, J. Ren, Mater. Des. 86 (2015) 922–932, https://doi.org/10.1016/j.matdes.2015.07.140.

[7] N.S. Neelam, S. Banumathy, C.M. Omprakash, D.V.V. Satyanarayana, A. Bhattacharjee, G.V.S. Nageswara Rao, Characterization of hot processing parameters of powder metallurgy TiAl-based alloy based on the activation energy map and processing map, Mater. Sci. Eng., A 839 (2022) 142769, https://doi.org/10.1016/j.msea.2022.142769.

[8] I. Egry, R. Brooks, D. Holland-Moritz, R. Novakovic, T. Matsushita, E. Ricci, S. Seetharaman, R. Wunderlich, D. Jarvis, Thermophysical properties of γ-titanium aluminide: the European IMPRESS project, Int. J. Thermophys. 28 (2007) 1026–1036, https://doi.org/10.1007/s10765-007-0219-6.

[9] K. Zhou, H.P. Wang, B. Wei, Determining thermophysical properties of undercooled liquid Ti–Al alloy by electromagnetic levitation, Chem. Phys. Lett. 521 (2012) 52–54, https://doi.org/10.1016/j.cplett.2011.09.061.

[10] R.K. Wunderlich, M. Mohr, Y. Dong, U. Hecht, D.M. Matson, R. Hyers, G. Bracker, J. Lee, S. Schneider, X. Xiao, H.J. Fecht, Thermophysical properties of the TiAl-2Cr-2Nb alloy in the liquid phase measured with an electromagnetic levitation device on board the International Space Station, ISS-EML, Int. J. Mater. Res. 112 (2021) 770–781, https://doi.org/10.1515/ijmr-2021-8266.

[11] R. Nowak, T. Lanata, N. Sobczak, E. Ricci, D. Giuranno, R. Novakovic, D. Holland-Moritz, I. Egry, Surface tension of γ-TiAl-based alloys, J. Mater. Sci. 45 (2009) 1993–2001, https://doi.org/10.1007/s10853-009-4061-z.

[12] C. Kenel, D. Grolimund, J.L. Fife, V.A. Samson, S. Van Petegem, H. Van Swygenhoven, C. Leinenbach, Combined *in situ* synchrotron micro X-ray diffraction and high-speed imaging on rapidly heated and solidified Ti–48Al under additive manufacturing conditions, Scripta Mater. 114 (2016) 117–120, https://doi.org/10.1016/j.scriptamat.2015.12.009.

[13] T.T. Xu, J.Y. Li, R.L. Xiao, J.Y. Qin, Y. Ruan, H. Li, The mixing enthalpy and liquid structural properties of Ti–Al alloys by ab inito molecular dynamics simulation, J. Phase Equilibria Diffus. 43 (2022) 585–593, https://doi.org/10.1007/s11669-022-01015-x.

[14] R. Fereidonnejad, A. Ostovari Moghaddam, M. Moaddeli, Modified embedded-atom method interatomic potentials for Al-Ti, Al-Ta, Al-Zr, Al-Nb and Al-Hf binary intermetallic systems, Comput. Mater. Sci. 213 (2022) 111685, https://doi.org/10.1016/j.commatsci.2022.111685.

[15] D. Farkas, C. Jones, Interatomic potentials for ternary Nb - Ti - Al alloys, Model. Simulat. Mater. Sci. Eng. 4 (1996) 23–32, https://doi.org/10.1088/0965-0393/4/1/004.

[16] Y.K. Kim, H.K. Kim, W.S. Jung, B.J. Lee, Development and application of Ni-Ti and Ni-Al-Ti 2NN-MEAM interatomic potentials for Ni-base superalloys, Comput. Mater. Sci. 139 (2017) 225–233, https://doi.org/10.1016/j.commatsci.2017.08.002.

[17] R.L. Xiao, K.L. Liu, Y. Ruan, B. Wei, Rapid acquisition of liquid thermophysical properties from pure metals to quaternary alloys by proposing a machine learning strategy, Appl. Phys. Lett. 123 (2023) 052204, https://doi.org/10.1063/5.0160046.

[18] R.E. Ryltsev, N.M. Chtchelkatchev, Deep machine learning potentials for multicomponent metallic melts: development, predictability and compositional transferability, J. Mol. Liq. 349 (2022) 118181, https://doi.org/10.1016/j.molliq.2021.118181.

[19] K. Sheriff, Y. Cao, T. Smidt, R. Freitas, Quantifying chemical short-range order in metallic alloys, Proc. Natl. Acad. Sci. 121 (2024) e2322962121, https://doi.org/10.1073/pnas.2322962121.

[20] T. Kim, B. Choi, Y. Jeong, D. Lee, M. Chang, Effects of annealing on tensile property and corrosion behavior of Ti–Al–Zr alloy, J. Nucl. Mater. 301 (2002) 81–89, https://doi.org/10.1016/S0022-3115(02)00710-9.

[21] M. Musi, S. Kardos, L. Hatzenbichler, D. Holec, A. Stark, M. Allen, V. Güther, H. Clemens, P. Spoerk-Erdely, The effect of zirconium on the Ti-(42-46 at.%)Al system, Acta Mater. 241 (2022), https://doi.org/10.1016/j.actamat.2022.118414.

[22] P.K. Sinha, Terminal solid solubility of hydrogen in an alpha-phase titanium alloy, Metall. Mater. Trans. A 54 (2023) 3112–3117, https://doi.org/10.1007/s11661-023-07081-1.

[23] Y. Zhang, H. Wang, W. Chen, J. Zeng, L. Zhang, H. Wang, W. E, Dp-Gen, A concurrent learning platform for the generation of reliable deep learning based potential energy models, Comput. Phys. Commun. 253 (2020) 107206, https://doi.org/10.1016/j.cpc.2020.107206.

[24] R.L. Xiao, K.L. Liu, Y. Ruan, L. Hu, B. Wei, Tutorial: deep learning prediction of thermophysical properties for liquid multicomponent alloys, J. Appl. Phys. 134 (2023) 191101, https://doi.org/10.1063/5.0173250.